Binding energies and structures of Ca-He_2 weakly bound triatomic complexes

David López-Durán, Rocío Rodríguez-Cantano, Tomás González-Lezana, Gerardo Delgado-Barrio, and Pablo Villarreal*
Instituto de Física Fundamental, IFF-CSIC, Serrano 123, 28006 Madrid, Spain

Franco A. Gianturco
Department of Chemistry and CNISM, University of Rome La Sapienza, Piazzale Aldo Moro 5, 00185 Rome, Italy
(Received 27 June 2012; published 1 August 2012)

Bound states of ^{40}Ca-^{n}He$_2$, $n = 3,4$, triatomic complexes are investigated. The potential-energy surface, represented as the addition of atomic-pair interactions, is that recently used to study these systems by Gou and Li, Phys. Rev. A **85**, 012510 (2012). The results obtained from three different methods, in fair agreement, profoundly disagree with those reported in the reference above. In addition, we address the feasibility of two Ca-He interactions existing in the literature by analyzing the characteristics of their ground and excited vibrorotational states. To this end, simulated absorption spectra in the region of microwaves are also presented and discussed.

DOI: 10.1103/PhysRevA.86.022501 PACS number(s): 31.15.ac, 33.15.Bh, 33.15.Fm

I. INTRODUCTION

Helium droplets provide an ideal matrix for spectroscopic studies due to their high cooling rate, low temperature, and weak interactions [1–4], and are nowadays routinely used for the spectroscopic characterization of molecules. Trimers formed with an atomic impurity and He atoms are usually interpreted as extreme limiting cases of larger droplets. The shifts of the electronic transition lines with respect to the isolated atom determine the location of the impurity attached to a droplet. The issue of establishing solvation instead of surface location for an impurity atom in a helium droplet is therefore of great importance to further understand the behavior of the spectroscopic observations as a function of the droplet's size. While most impurities (atomic and molecular) are found to reside in the interior [5], it is also well established that according to the model of Ref. [6], alkali-metal atoms preferentially reside in a "dimple" at the surface of the drops for both helium isotopes [3,7]. In turn, the borderline character for the solvation properties of alkaline-earth atoms in He droplets requires the use of high-quality impurity-He pair interaction potentials. Excitation spectra of alkaline-earth atoms attached to helium nanodroplets have been recorded using laser-induced fluorescence spectroscopy [8–10], and more recently through a variety of spectroscopic techniques applied to the analysis of the excited state [11]. In particular, it has been established that Ca atoms reside on the surface of superfluid boson helium nanodroplets [9], in agreement with density functional theory calculations [12].

In this sense, the study of the preferences shown by the impurities regarding their precise location with respect to the surrounding pair of He atoms in the trimer is expected to provide some light into the intrinsic nature of its interaction with the rare gas. As commonly accepted, the weakness of these interactions allows one to represent the potential-energy surface (PES) as a simple sum of two-body (2B) potentials. While the potential describing the He-He forces within the droplet is well established [13], there are several studies describing the Ca-He interaction. Besides some previous works on the subject, the potentials by Lovallo and Klobukowski [14] and by Kleinekathöfer [15] turn out to be the ones commonly used. Whereas the former exhibits an equilibrium distance of about 10 a_0 and a depth of almost 15 K, the potential of Ref. [14] indicates that the Ca-He well has a minimum shifted to a slightly larger equilibrium distance and has a much shallower depth of about 5 K.

The interest in the existing potentials for describing the interactions within the triatomics under study here has been renewed by recent investigations performed by Gou and Li [16], who employed the Ca-He potential of Ref. [15] to calculate the bound states of the Ca-He_2 system. According to their results, both the fermionic (formed with two ^{3}He atoms) and the bosonic (formed with ^{4}He atoms) clusters are capable of supporting several such states. However, as indicated elsewhere [17], some of the reported binding energies seem to be at odds with respect to the corresponding dissociation limits and, for the case of Ca-$^4He_2$, with the global minimum of the PES. A similar investigation [18] with the weaker Ca-He potential by Lovallo and Klobukowski [14] reveals the existence of a pair of bound states for both isotopic variants, with noticeably smaller binding energies than those observed for the potential of Ref. [15]. Here, in an attempt to shed some light on the reliability of the intriguing results reported by Gou and Li [16], we present three different calculations on the bound levels, and on their corresponding structures, for bosonic Ca-$^4He_2$ and fermionic Ca-$^3He_2$ complexes. In addition, we try to clarify the situation with respect to the differences in the Ca-He interaction as described by the two above-mentioned potentials. We further estimate the energy levels for rotationally excited trimers and simulate their absorption spectra within the electric dipole approximation, which is data that could serve as guidance for possible experimental observations to be carried out on the present system.

The paper is organized as follows: The next section briefly describes the intermolecular forces employed in the present study, while Sec. III provides details on our theoretical methods. Section IV presents and discusses the results we have obtained on Ca-$^4He_2$ and Ca-$^3He_2$ complexes, while Sec. V summarizes our conclusions.

*Corresponding author: p.villarreal@csic.es

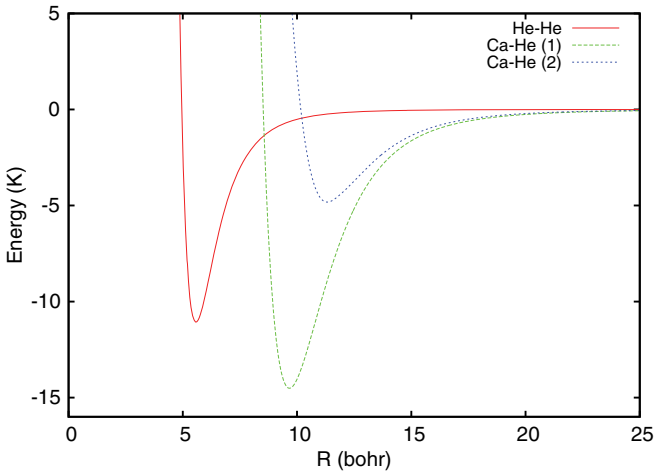

FIG. 1. (Color online) Interatomic-energy potentials for He-He [19] and Ca-He systems. Ca-He(1): Ref. [15]; Ca-He(2): Ref. [14].

II. THE INTERACTION POTENTIALS

The PES is represented as a simple sum of two-body (2B) potentials,

$$V_{\rm TOT}(R_1,R_2,R_3) = V_{\rm Ca-He}(R_1) + V_{\rm Ca-He}(R_2) + V_{\rm He-He}(R_3). \tag{1}$$

For the He-He interaction potential, we have selected the analytical form suggested by Aziz and Slaman [19], which takes advantage of several features of the experimental data and which has been employed several times already in our previous studies of similar clusters [20]. As mentioned in Sec. I, the Ca-He interaction chosen here is that of Kleinekathöfer [15], which is also given in analytical form.

Figure 1 displays the He-He [19] and Ca-He [15] interatomic potentials used in this work. For comparison, the Ca-He potential [14] recently used by us [18] is also included in this figure. As can be seen, the previously used Ca-He interaction [14] presents its equilibrium distance at around 12 a_0 and a well depth near 5 K, while these quantities are $\sim$5 a_0 and $\sim$12 K, respectively, for the He-He interaction. Within a classical picture, the situation suggested indicates a closer packing of the two helium atoms that then push out the calcium partner [18]. This is not so clear for the Ca-He interaction [15] considered here, which shows an equilibrium distance around 10 a_0 and a well depth near 15 K. Nevertheless, the bottom of the present PES should be ~ -42 K, and no bound states lower in energy than this magnitude should be found. Hence, and even for a totally rigid Ca-He$_2$ complex, the energy value reported for the ground level of the bosonic system in Ref. [16] becomes unphysical.

III. THEORETICAL METHODS

A. Discrete variable representation in satellite coordinates

The Hamiltonian describing the Ca-He$_2$ triatomic system can be written in satellite coordinates $\{\boldsymbol{R}_k\}$, after separation of the center-of-mass motion, as [21]

$$H = \sum_{k=1}^{2}\left[-\frac{\hbar^2}{2\mu}\frac{\partial^2}{\partial R_k^2} + \frac{\boldsymbol{l}_k^2}{2\mu R_k^2} + V_{\rm Ca-He}(R_k)\right] + V_{\rm He-He}(R_1,R_2,\cos\gamma) - \frac{\hbar^2}{m_{\rm Ca}}\nabla_{\boldsymbol{R}_1}\cdot\nabla_{\boldsymbol{R}_2}, \tag{2}$$

where $\boldsymbol{R}_k$ are the vectors from the Ca atom to the different He atoms, $\boldsymbol{l}_k$ are the angular momenta associated with $\boldsymbol{R}_k$, μ is the reduced mass of the Ca-He system, and $\cos\gamma = \boldsymbol{R}_1\cdot\boldsymbol{R}_2/R_1R_2$. In a space-fixed coordinate system, we consider the following basis functions:

$$\phi^{LM}_{q_1q_2}(\boldsymbol{R}_1,\boldsymbol{R}_2) = f_{m_1}(R_1)f_{m_2}(R_2)\mathcal{Y}^{LM}_{\ell_1\ell_2}(\hat{\boldsymbol{R}}_1,\hat{\boldsymbol{R}}_2), \tag{3}$$

where the f_{m_i} functions, associated with the Ca-He vibrations, are the fixed-node functions of Muckerman [22] leading to a discrete variable representation (DVR). They have been recently detailed [18]. In Eq. (3), $\mathcal{Y}^{LM}_{\ell_1\ell_2}$ are angular functions in the coupled representation,

$$\mathcal{Y}^{LM}_{\ell_1\ell_2}(\hat{\boldsymbol{R}}_1,\hat{\boldsymbol{R}}_2) = (-1)^L\sqrt{2L+1}\sum_{\omega}\begin{pmatrix}\ell_1 & \ell_2 & L\\ -\omega & \omega-M & M\end{pmatrix} \times Y_{\ell_1\omega}(\theta_1,\phi_1)Y_{\ell_2 M-\omega}(\theta_2,\phi_2), \tag{4}$$

where $\hat{\boldsymbol{R}}_k = \boldsymbol{R}_k/R_k = (\theta_k,\phi_k)$ are unit vectors, $\begin{pmatrix}\cdots\\ \cdots\end{pmatrix}$ are 3-j symbols, and $Y_{\ell_k\omega}$ are spherical harmonics. L is the quantum number associated with the total angular momentum $\boldsymbol{L} = \boldsymbol{l}_1 + \boldsymbol{l}_2$ with third component M, and ℓ_k and m_k ($k = 1,2$) are quantum numbers associated with the angular momenta $\boldsymbol{l}_k$ and the Ca-He vibrations, respectively, and are collected into a set of quantum numbers $\{q_k\} = \{m_k\ell_k\}$.

Further, one builds up a symmetry-adapted basis set of functions:

$$\psi^{LM\varepsilon\kappa}_{q_1q_2} = \left[2(1+\delta_{m_1m_2}\delta_{\ell_1\ell_2})\right]^{-1/2}\left[\phi^{LM}_{q_1q_2} + \varepsilon\kappa(-1)^L\phi^{LM}_{q_2q_1}\right], \tag{5}$$

which are eigenfunctions of $\mathcal{E}^*$, the inversion, and $\mathcal{P}$, the permutation of the He atoms, with eigenvalues $\varepsilon = (-1)^{\ell_1+\ell_2}$ and κ, respectively [18]. Matrix elements of the Hamiltonian of Eq. (2), as well as expressions for probability distributions of the variables R ($R = R_1$ or R_2), $\cos\gamma$, or R_3, can be found in Ref. [23]. The eigenstates of H are then of the form

$$\Psi^{LM\varepsilon\kappa}_{v} = \sum_{q_1q_2} a^{(v)}_{q_1q_2}\psi^{LM\varepsilon\kappa}_{q_1q_2}, \tag{6}$$

with associated energies $E^{L\varepsilon\kappa}_v$, which are degenerate in M.

The existence of absorption spectra, or their numerical simulation, could shed some light on the comparative physical feasibility of the two different Ca-He interactions [14,15]. Using first-order perturbation theory in the dipole approximation, the simulated absorption spectrum would consist of lines of intensity,

$$I(v'L'M'\varepsilon'\kappa' \leftarrow vLM\varepsilon\kappa) \propto \left|\left\langle\Psi^{LM\varepsilon\kappa}_{v}|\boldsymbol{\mu}\cdot\boldsymbol{e}|\Psi^{L'M'\varepsilon'\kappa'}_{v'}\right\rangle\right|^2, \tag{7}$$

where $\boldsymbol{\mu}$ is the dipole moment, and $\boldsymbol{e}$ is the electric field, at an energy of the incident photon $\hbar\omega = E^{L'\varepsilon'\kappa'}_{v'} - E^{L\varepsilon\kappa}_{v}$.

We have resorted to model the dipole moment as well as to perform a simple estimate of the intensities of the

possible transitions. As an essentially nonlinear molecule, taking into account that calcium is more polarizable than helium and fixing—in spite of its inherent floppiness—the R_1 and R_2 Ca-He distances at the position of the peaks of the corresponding distributions (see below), the bending motion (oscillations in γ) should produce an effective dipole moment along the bisectrix of the He-$\widehat{\text{Ca}}$-He γ angle with separated positive and negative charges, with the former being near the Ca atom and the latter being near the middle of the He-He distance, i.e., proportional to $\boldsymbol{R}_1 + \boldsymbol{R}_2$,

$$\boldsymbol{\mu} \propto \cos(\gamma/2)\,(\hat{\boldsymbol{R}}_1 + \hat{\boldsymbol{R}}_2). \tag{8}$$

We assume linear polarization of the electric field. Choosing the space-fixed Z axis along the direction of polarization, the relevant transition moment becomes

$$\boldsymbol{\mu}\cdot\boldsymbol{e} = \mu_Z \propto \cos(\gamma/2)\,(\cos\theta_1 + \cos\theta_2), \tag{9}$$

to be included in Eq. (7). According to the modeling of $\boldsymbol{\mu}$, with the Ca-He distances being kept fixed, the calculation of the transition intensities therefore reduces to estimating integrals of the form

$$\begin{aligned}&\langle \mathcal{Y}^{LM}_{\ell_1\ell_2} | \cos(\gamma/2)\,(\cos\theta_1 + \cos\theta_2) | \mathcal{Y}^{L'M'}_{\ell'_1\ell'_2}\rangle \\ &\quad = \sum_{JKj_1j_2} \langle \mathcal{Y}^{LM}_{\ell_1\ell_2} | \cos(\gamma/2) | \mathcal{Y}^{JK}_{j_1j_2}\rangle \langle \mathcal{Y}^{JK}_{j_1j_2} | \cos\theta_1 + \cos\theta_2 | \mathcal{Y}^{L'M'}_{\ell'_1\ell'_2}\rangle,\end{aligned} \tag{10}$$

where the identity has been introduced to allow for the separation into products of analytical integrals [23]. Indeed, by expanding in Legendre polynomials $\cos(\gamma/2) = \sum_\lambda c_\lambda P_\lambda(\cos\gamma)$, and noting that $\cos\theta = P_1(\cos\theta)$, one arrives at (see, e.g., Eqs. (27) and (30) of Ref. [23])

$$\langle \mathcal{Y}^{LM}_{\ell_1\ell_2} | P_\lambda(\cos\gamma) | \mathcal{Y}^{JK}_{j_1j_2}\rangle = \delta_{LJ}\delta_{MK}(-1)^{\ell_1-j_1+L} A(\ell_1,\ell_2,j_1,j_2) \begin{Bmatrix} \ell_1 & \lambda & j_1 \\ j_2 & L & \ell_2 \end{Bmatrix} \begin{pmatrix} \ell_1 & \lambda & j_1 \\ 0 & 0 & 0 \end{pmatrix} \begin{pmatrix} \ell_2 & \lambda & j_2 \\ 0 & 0 & 0 \end{pmatrix} \tag{11}$$

and

$$\langle \mathcal{Y}^{LM}_{j_1j_2} | P_1(\cos\theta_1) | \mathcal{Y}^{L'M'}_{\ell'_1\ell'_2}\rangle = \delta_{MM'}\delta_{j_2\ell'_2}(-1)^{j_2} A(L,L',j_1,\ell'_1) \begin{Bmatrix} j_1 & L & \ell'_2 \\ L' & \ell'_1 & 1 \end{Bmatrix} \begin{pmatrix} \ell'_1 & 1 & j_1 \\ 0 & 0 & 0 \end{pmatrix} \begin{pmatrix} L & 1 & L' \\ M & 0 & -M \end{pmatrix}, \tag{12}$$

and something similar for the integrals involving $P_1(\cos\theta_2)$ by exchanging j_1 by j_2 and ℓ'_1 by ℓ'_2. In Eq. (12), the δ_{LJ} and δ_{MK} appearing in Eq. (11) have been already taken into account, $\{\vdots\}$ are 6-j symbols, and, in both equations, the A coefficients are $A(k,l,m,n) = \sqrt{(2k+1)(2l+1)(2m+1)(2n+1)}$. The presence of the last 3-j symbol in Eq. (12) ensures that only $L' = L, L\pm 1 \leftarrow L$ ($0 \not\leftarrow 0$) transitions become allowed. Also, by accounting for symmetry-adapted functions, and after some algebra, the additional selection rules $\kappa' = \kappa$ and $\varepsilon' = -\varepsilon$ are readily obtained.

B. Distributed Gaussian functions method

The distributed Gaussian functions (DGF) method [24–26] has been employed before for different systems with two identical rare-gas atoms and an impurity atom, as in the Li-He$_2$ [20], He$_2$-H$^-$ [27] and Ne$_2$-H$^-$ [28] complexes. The total Hamiltonian in this approach (for a zero total angular momentum) can be expressed via atom-atom coordinates as

$$\begin{aligned}H(R_1,R_2,R_3) = {}& \frac{-\hbar^2}{2\mu_{\text{Ca-He}}} T_1 + \frac{-\hbar^2}{m_{\text{Ca}}} T_2 \\ &+ \sum_{i=1}^{2} V_{\text{HeCa}}(R_i) + V_{\text{HeHe}}(R_3).\end{aligned} \tag{13}$$

The corresponding expressions for the T_1 and T_2 kinetic operators in terms of the interparticle coordinates, i.e., R_1 and R_2 for the two Ca-He distances and R_3 for the He-He distance, are given explicitly in Ref. [20].

Within the DGF framework, the total wave function is expanded as follows:

$$\Phi_{\text{k}}(R_1,R_2,R_3) = \sum_j a_j^{(\text{k})} \phi_j(R_1,R_2,R_3), \tag{14}$$

where

$$\phi_j(R_1,R_2,R_3) = N_{lmn}^{-1/2} \sum_{P\in S_2} P[\varphi_l(R_1)\varphi_m(R_2)]\varphi_n(R_3), \tag{15}$$

and the basis is symmetrized by means of the proper P permutation operator for the R_1 and R_2 coordinates. Here, j denotes a collective index such as $j = (l \leqslant m; n)$.

The corresponding normalization constants N_{lmn} are

$$N_{lmn} = 2s_{nn}\left(s_{ll}s_{mm} + s_{lm}^2\right), \tag{16}$$

expressed in terms of the overlap integrals

$$s_{pq} = \langle \varphi_p | \varphi_q \rangle. \tag{17}$$

The φ_p functions are chosen to be DGFs centered at the R_p position [29], and the products $\varphi_l\varphi_m\varphi_n$ are included in the basis set if the corresponding centers verify the triangle requirement

$$|\, R_l - R_m \,| < R_n < R_l + R_m. \tag{18}$$

One can calculate probability density functions by integrating in the corresponding coordinates the squared modulus of the total wave function given Eq. (14), while it is also possible to gain further information regarding the structure of the bound states by means of evaluating the so-called pseudoweights $P_j^{(k)}$ defined as

$$1 = \langle \Phi_{\text{k}} \mid \Phi_{\text{k}} \rangle = \sum_j a_j^{(k)} \langle \Phi_k \mid \phi_j \rangle = \sum_j P_j^{(k)}. \tag{19}$$

TABLE I. DMC and DVR calculated energies (cm^{-1}) of the bound states for the two He-Ca dimers indicated. These energies were obtained using the Ca-He interaction of Ref. [15] (in parentheses, energies coming from the use of shallower Ca-He potential [14]).

	DMC	DVR
Ca-^{3}He	-3.2950 ± 0.0007 (-0.362 ± 0.004)	-3.2945(-0.3575)
Ca-^{4}He	-3.9104 ± 0.0006 (-0.5427 ± 0.0006)	-3.9107(-0.5450)

These quantities, associated to each basis set function ϕ_j, can be employed to estimate the total contribution of the different kind of triangular structures in the average geometry of any trimer bound state.

Following previous studies, we have used a DGF-based approach to investigate the rotating system [25,30,31]. Within this scheme, the total Hamiltonian is partitioned into a rotationless and purely vibrational part, $H_{\rm vib}$, given in Eq. (13), and into the rotational part, $H_{\rm rot}$, corresponding to an asymmetric rigid rotor [32–34], as $H_{\rm tot} = H_{\rm vib} + H_{\rm rot}$. Once the $J = 0$ problem is solved, the corresponding eigenstates are employed, together with standard rotational functions expressed in terms of Ω and M, the projections of $\mathbf{J}$ on the body- and space-fixed z axis, respectively, to build the basis sets which diagonalize the rotational part [30,31]. The reference system to describe the rotating system including its vibration is chosen to verify the Eckart conditions [35,36] in a similar way as the one followed in our previous work on the Ne_2-H^- system [28].

C. Quantum Monte Carlo methods

The quantum stochastic simulation employed here has been used previously (see Refs. [37–39], for instance) and we therefore present here only a brief outline of it. It is formed by a pure variational Monte Carlo (VMC) calculation followed by a diffusion Monte Carlo (DMC) approach. In the VMC step, the energy is optimized with respect to the parameters of the trial wave function $\Psi_T(\mathbf{R})$, which in the case of a system formed by an impurity and N helium atoms can be expressed as the product of purely nodeless exponential forms [38],

$$\Psi_T(\mathbf{R}) = \Psi_{\rm Ca-He}(\mathbf{R})\Psi_{\rm He-He}(\mathbf{R}). \tag{20}$$

$\mathbf{R} \equiv \{\boldsymbol{R}_i\}_{i=1}^N$ is the collective index that brings together the coordinates $\boldsymbol{R}_i$ of the rare-gas particles, while $\Psi_{\rm Ca-He}(\mathbf{R})$ and $\Psi_{\rm He-He}(\mathbf{R})$ are the Ca-He and the He-He parts of the wave function, respectively:

$$\Psi_{\rm Ca-He}(\mathbf{R}) = \prod_{i=1}^{N} \varphi_{\rm Ca-He}(R_i), \tag{21}$$

$$\Psi_{\rm He-He}(\mathbf{R}) = \prod_{j=1,k=j+1}^{j=N-1,k=N} \varphi_{\rm He-He}(R_{jk}). \tag{22}$$

$R_i \equiv |\boldsymbol{R}_i|$, $R_{jk} \equiv |\boldsymbol{R}_j - \boldsymbol{R}_k|$ and $\varphi(\cdot) = \exp\{-f(\cdot)\}$, with f as the Jastrow functions whose variable and parameters depend on whether we are considering the Ca-He or the He-He interactions, respectively:

$$f(R) = \left(\frac{p_5}{R}\right)^5 + \left(\frac{p_3}{R}\right)^3 + \left(\frac{p_2}{R}\right)^2 + p_1 R + p_0 \ln(R). \tag{23}$$

The diffusion equation associated with the Hamiltonian (2), expressed in Cartesian coordinates, is now solved by considering Eq. (20) as the trial wave function. The calculation is performed N_w times, and each of these simulations is called a replica or a *walker*. The DMC stage relies on the short-time approximation [40] and now the addition of weights to the walkers corrects the variational estimate towards a more realistic expectation value (with the wave function fixed). The imaginary time evolves a quantity $\triangle\tau$ on each step. After a large enough number of M steps, the distribution function stabilizes at its ground state $\Psi_0\Psi_T$ ("mixed estimator") [41–43].

IV. RESULTS

A. Numerical details

The employed masses were $m(\mathrm{Ca}) = 40.07878$, $m(^4\mathrm{He}) = 4.0026$, and $m(^3\mathrm{He}) = 3.01604$ amu. For comparisons, the conversion factors 1 K = 0.69503877 cm^{-1} and $1a_0 = 0.52917726$ Å have been employed.

TABLE II. $L = 0$ bound energies (cm^{-1}) obtained by means of DMC, DVR, and DGF calculations for the indicated trimers, using the Ca-He interaction of Ref. [15]. In parentheses, the corresponding values produced by using the Ca-He potential form of Ref. [14]. The * signifies $S = 0$ singlet states.

	v	DMC	DVR	DGF
Ca-^{3}He$_2{}^*$	0	-6.6566 ± 0.0002 (0.778 ± 0.002)	-6.6531 (-0.7631)	-6.6517 (-0.7633)
	1		-5.8313 (-0.3840)	-5.8711 (-0.3835)
	2		-4.0952	-4.1450
Ca-^{4}He$_2$	0	-7.9869 ± 0.0019 (-1.2242 ± 0.009)	-7.9868 (-1.2174)	-7.9699 (-1.2226)
	1		-7.3210 (-0.8663)	-7.3344 (-0.8916)
	2		-5.8831	-5.8932
	3		-3.9920	-4.0140

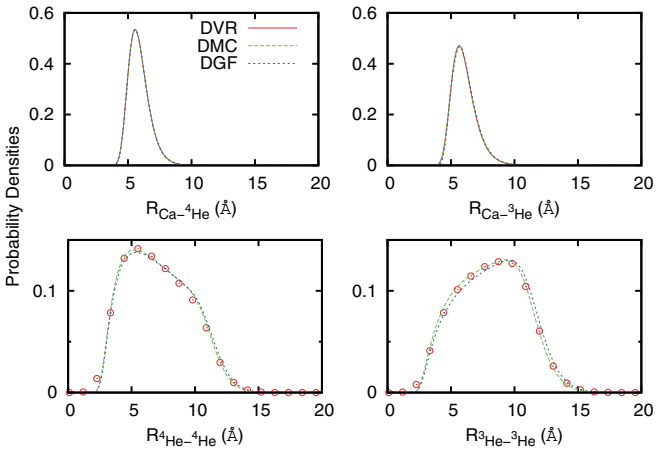

FIG. 2. (Color online) $L = 0$ radial distributions of the Ca-He and He-He distances for the ground states of the two Ca-^{n}He$_2$ complexes obtained by the three different computational methods of the present work and using the Ca-He interaction of Ref. [15]. Left panels: bosonic system; right panels: fermionic (singlet) system. Red points in the He-He distance distributions correspond to DVR estimations, assuming the independence of probability densities in Ca-He distances and cosγ [18].

In the variational DVR treatment using satellite coordinates, we have considered 25 points of R in the interval $[5,25]a_0$. For total angular momenta $L = 0$ and 1, and for boson as well as for singlet or triplet fermion systems, up to 31 values, from 0 to 30, of ℓ_1 and ℓ_2 were accounted for, while 101 points of a Gauss-Legendre quadrature in the interval $[-1,1]$ were used to describe the He-He interaction in terms of R_1, R_2, and $\cos\gamma = \hat{\boldsymbol{R}}_1 \cdot \hat{\boldsymbol{R}}_2$. In this way, energy convergence up to the second decimal figure (cm^{-1}) was achieved for ground vibrational states, or up to the first one for excited states.

With respect to the VMC part, we have used the Powell method [44] along a total of $M = 5 \times 10^5$ steps to find the

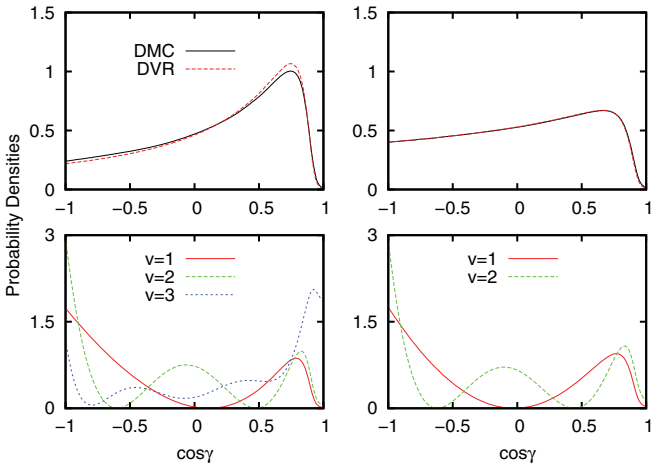

FIG. 3. (Color online) Angular distributions for $L = 0$ states of the Ca-^{4}He$_2$ complex (left panels) and singlet fermionic Ca-^{3}He$_2$ system (right panels). The upper panels show DMC-DVR results for the corresponding $v = 0$ ground levels, while the lower panels depict DVR results for the excited states. The Ca-He interaction used was that of Ref. [15].

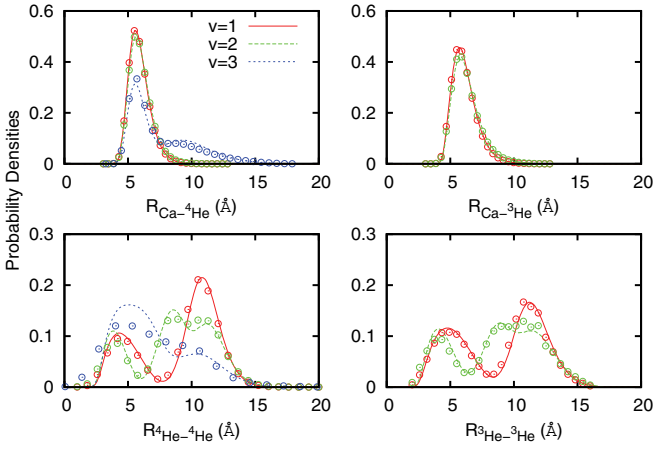

FIG. 4. (Color online) $L = 0$ radial distributions of the Ca-He and He-He distances for the excited states of the two Ca-^{n}He$_2$ complexes obtained through DGF (lines) and DVR (points) methods. Left panels: bosonic system; right panels: singlet fermionic system. Ca-He interaction [15] was used.

absolute minimum of the trial wave function Ψ_T in the space formed by a total of 10 parameters, i.e., five each of He-impurity and He-He interactions. The number of walkers N_w ranged between 500 and 4000, sampled in their propagation through a Langevin procedure, with the variance of E_L as the cost function to minimize [38,45]. In the DMC stage of the calculations, a similar number of steps have been used; as $10 \leqslant \triangle\tau \leqslant 300$ hartree^{-1}, a total of $5 \times 10^7 - 3 \times 10^8$ hartree^{-1} has been considered, which is a time long enough for all of the quantities to have reached convergence. The branching scheme for the walkers was that proposed by Blume *et al.* [46]. For

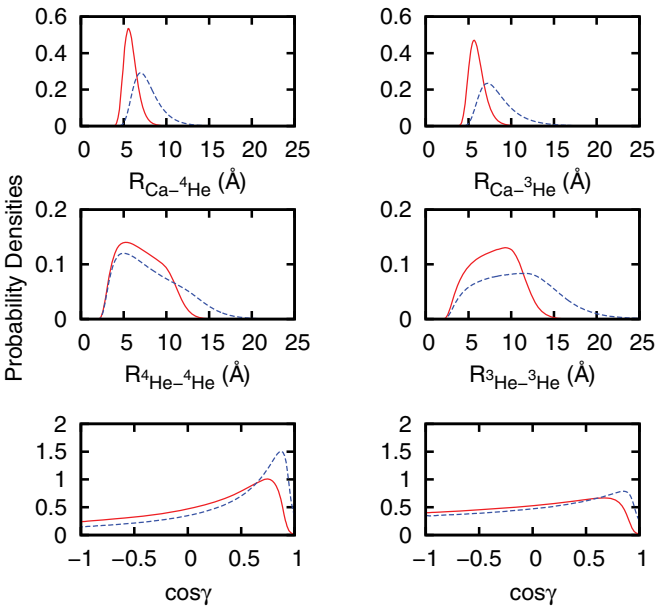

FIG. 5. (Color online) DMC normalized distributions of different magnitudes corresponding to the ground state of the Ca-^{4}He$_2$ (left panels) and Ca-^{3}He$_2$ ($S = 0$, right panels) species obtained using the Ca-He interaction of Ref. [15] (solid lines) or that of Ref. [14] (dashed lines).

TABLE III. Geometrical quantities for the ground level of the indicated species estimated through the DMC distributions of Fig. 5; see text. They depend on the Ca-He interaction used: first entry is that of Ref. [15]; second one is the interaction of Ref. [14]. d is the distance from Ca to the center of mass of He_2.

	$R_1 = R_2$ (Å)	R_3 (Å)	d (Å)	γ (deg)	weight (%)
	5.7, 7.2	10.0, 11.7	2.7, 4.2	123, 109	57, 63
Ca-$^3He_2$*	5.7, 7.2	4.6, 4.9	5.2, 6.8	48, 40	43, 37
	5.6, 7.0	4.2, 4.2	5.2, 5.7	44, 35	63, 73
Ca-$^4He_2$	5.6, 7.0	9.8, 11.3	2.7, 4.1	122, 108	37, 27

a fixed N_w, we have fitted the energy to a simple straight line, $E = m \times \triangle\tau + n$, which tends to n when $\triangle\tau \to 0$. The couples (N_w,n) have been extrapolated, in turn, to the function $y = a + b/N_w$. The parameter we are interested in is a, which is the value of the energy when the number of walkers tends to infinity. The errors presented in Tables I and II correspond to the error associated with the fitting of a. All of the shown geometry distributions belong to the calculations with $N_w = 4000$ and $\triangle\tau = 300$ hartree^{-1}.

For the DGF calculation, 32 Gaussian functions with centers between 4 a_0 and 35 a_0, with a distance of 1a_0 between consecutive DGFs, were chosen for the He-He distances (R_3), whereas for the two He-Ca distances (R_1 and R_2) and given the difference between the position of the corresponding interparticle potentials (see Fig. 1), the center of the first DGF was taken at 8 a_0. With this choice, a total number of 9181 ϕ_j basis functions in the expansion of Eq. (14) was taken into account. A numerical grid of 5000 points between 0.5 a_0 and 47 a_0 were considered for the numerical integrations.

B. Ca-He dimers

In Table I, we present energies of the bound levels found through DMC and DVR calculations for the Ca-^{3}He and Ca-^{4}He dimers. At each entry, the first row corresponds to the results obtained using the Ca-He interaction of Ref. [15], while the second row shows the values achieved [18] when using the form of Ref. [14] for representing that dimer. As can be seen, both methods lead to identical results for each potential considered. The values produced by the Ca-He interaction [15], −4.740 K and −5.626 K for the lighter and heavier helium isotope, respectively, agree with those reported in Ref. [16]. As expected, when considering the less deep Ca-He potential of Ref. [14], the energies of the two isotopes become almost one order of magnitude less bound.

C. $L = S = 0$ Ca-He_2 trimers

For nonrotating ($L = 0$) boson and singlet (total nuclear spin $S = 0$) fermion Ca-He_2 systems, we list in Table II the energies associated with bound levels when the Ca-He interaction of Ref. [15], or in parentheses that of Ref. [13], are used. No triplet fermionic bound states were found at $L = 0$. Indeed, the three methodologies yield essentially the same results, which thus provide a good level of reliability for the present methods. They are measured with respect to the total dissociation, i.e., the Ca+He+He asymptotic limit, and are below the energy of the corresponding Ca-He dimer. When using the Ca-He interaction of Kleinekathöfer [15], three bound-state levels are supported by the fermionic system, while the bosonic one supports four bound levels, with the last one being close to the dissociation limit. The energies of $v = 0$ ground levels are nearly two times those of the Ca-He species, according to an independent particle (IP) model [18,47], in such a way that the concerted He rotations around Ca roughly compensate the He-He interaction. The next two bound levels, $v = 1$ and 2, correspond in the two systems to pure bending excitations, as will be shown below, while the bosonic $v = 3$ level describes a mixed stretching-bending excitation. Apart from the mass effect, bosonic and singlet fermionic nonrotating species are very similar, as their spatial wave functions should be totally symmetric, and the corresponding energies do not differ too much. The present results are completely different from those of Gou and Li [16] who report four bound levels for the fermionic complex, although three of them were above the Ca-^{3}He+He dissociation limit, and 31 bound levels for the bosonic complex (the first one was below the global minimum of the PES, as already mentioned, and up to 27 levels above the corresponding dissociation limit).

In Fig. 2, we depict distributions in the Ca-He and He-He distances of the $v = 0$ ground states corresponding to the nonrotating ($L = 0$) Ca-$^4He_2$ and Ca-$^3He_2$ ($S = 0$) complexes. They were obtained using the Kleinekathöfer Ca-He potential form [15]. As it occurred for the calculated energies, all three methods employed here yield almost identical results, which again provides some proof of numerical reliability. For Ca-He distances, bosonic and singlet fermionic distributions peak at ∼6 Å, although the latter slightly extends to longer distances. The distributions of He-He distances are clearly broader, and the bosonic one peaks at ∼6 Å, while the fermionic does at ∼10 Å, denoting an acute isosceles, almost equilateral, equilibrium configuration for the former complex and an obtuse isosceles arrangement for the latter.

TABLE IV. Contribution of the different triangle geometries included in the DGF basis set to the average structure of the ground state for the Ca-$^4He_2$ and Ca-$^3He_2$ systems according to the DGF calculation. Ca-He interaction is of Ref. [15].

Triangle	Ca-$^4He_2$	Ca-$^3He_2$
Equilateral	9%	6%
Isosceles A	33%	28%
Isosceles B	8%	8%
Quasilinear A	13%	22%
Quasilinear B	0%	0%
Scalene	37%	36%

TABLE V. $L = 1$ DVR vibrational energies (cm^{-1}) for the different systems studied using the Ca-He potential of Ref. [15] (first entry) or that of Ref. [14] (second entry). The symmetry quantum numbers ε, κ are included for each system. The * represents $S = 0$ singlet states; the ** represents $S = 1$ triplet states.

v	Ca-^{4}He$_2$ ($\varepsilon = -1, \kappa = +1$)	Ca-^{3}He$_2$* ($\varepsilon = -1, \kappa = +1$)	Ca-^{3}He$_2$** ($\varepsilon = -1, \kappa = -1$)
0	−7.7344, − 1.042	−6.2781, − 0.5639	−6.3243, − 0.5517
1	−6.6287, ⋯	−4.9673, ⋯	−5.4143, ⋯
2	−4.8468, ⋯		−3.6508, ⋯

Angular distributions in terms of cosγ for the states reported in Table II are shown in Fig. 3. They were obtained through DMC ($v = 0$ states) and DVR (ground and excited vibrational states) procedures using the Ca-He interaction of Ref. [15]. Again, both results, for $v = 0$ (upper panels), are in excellent agreement, even better for fermions than for bosons. The latter present a preference for small angles, while the former are almost isotropic. As already mentioned, the DVR distributions of excited states (lower panels) show clear nodal structures for $v = 1$ and 2 in both species, and together with the corresponding DGF-DVR distributions in the Ca-He distances shown in the upper panels of Fig. 4, which are almost identical to those of the ground states shown by Fig. 2, denote that these states correspond to bending excitations. The bosonic $v = 3$ state, in turn, results from a mixed bending-stretching excitation; see left lower panel of Fig. 3 and left upper panel of Fig. 4.

The lower panels of Fig. 4 display DGF-DVR distributions in the He-He distances for excited states of the bosonic complex (left panel) and the singlet fermionic one (right panel). We like to note that these DVR results are approximate in that they were obtained in the frame of the IP model, i.e., by assuming the independence of the (exact) DVR distributions in Ca-He distances and in cosγ. Hence, in spite of the fact that the IP approach is able to best describe essentially the maxima and minima of the exact DGF distributions, we clearly see that it also behaves correctly for the ground and first excited states of bosons and fermions, while worsening as the excitation increases.

More indications regarding the overall geometry of the bound states of the title system can be gleaned from the probability densities shown in Fig. 5. In particular, we have fitted the distributions of the He-He distance, R_3, for the ground states of both Ca-^{3}He$_2$ and Ca-^{4}He$_2$ complexes (middle panels of Fig. 5) to two asymmetric Gaussian functions. Values of the distance d between the Ca atom and the center of mass of the cluster and of the average value of the γ angle have been calculated considering two possibilities for R_3: the location of the two Gaussian functions employed in such fitting, whose contribution to the overall probability density is shown in the last column of Table III. Values obtained with the Ca-He potential of Refs. [15] and [14], respectively, are shown separately in each entry of the table. Taking R_3 as the most probable value for the He-He distance, the maximum with the largest weight, estimates of d and the γ angle in the case of Ca-^{3}He$_2$ are ∼3 Å and ∼120°, respectively, for the He-Ca potential from Kleinekathöfer [15]. For the potential from Lovallo *et al.* [14], these values become ∼4 Å and 110°, respectively. Results obtained in the case of the Ca-^{4}He$_2$ system are slightly different, however, with the d distances increasing up to 5.2–5.7 Å for potentials from Refs. [15] and [14], respectively, and the γ angle taking values of 44° or 35° depending on the employed potential. These are indications that for the bosonic cluster, the Ca atom stays outside the helium atoms, which in turn tend to pack closer to each other, whereas Ca gets closer to the half distance of the helium atoms when these are ^{3}He, a feature which constitutes a signature of solvation. This scenario is common for both Ca-He interactions, although more pronounced in the case of the potential of Lovallo-Klobukowski [14] than for that of Kleinekathöfer [15].

These geometrical considerations can be further analyzed by means of the pseudoweights defined in Eq. (19) within the context of the DGF method. The analysis of the contribution of the different triangular arrangements existing in the basis set defined by the ϕ_j functions of the DGF calculation is shown for the ground state of the Ca-^{4}He$_2$ and Ca-^{3}He$_2$ systems in Table IV. In the table, isosceles A corresponds to those isosceles triangles in which both He-Ca distances are equal ($R_1 = R_2 \neq R_3$), whereas isosceles B refers to those arrangements in which the smallest He-Ca distance is equal to the He-He distance ($R_1 = R_3 \neq R_2$). Analogously, quasilinear A corresponds to those almost linear structures in which the Ca atom is located in between the two He atoms ($R_1 + R_2 \sim R_3$), whereas by quasilinear B we refer to those arrangements in which the Ca atom is at one of the extremes of the almost linear structure formed by the three atoms ($R_1 + R_3 \sim R_2$).

Results from Table IV indicate that for both isotopic variants, the most favorable structure of the system consists of scalene triangles. However, the noticeable contribution from the isosceles A and quasilinear A families should be interpreted as due to the important role played by those configurations with the Ca atom showing to locate itself in between both He atoms, on and off the coordinate He-He. This result seems to be consistent with the interpretation made above in terms of the strict maximum peaks observed for the probability densities of Fig. 2. In that figure, nevertheless, the broad maximum for the He-He distance could be due to the apparent elongation on the He-He distance with respect to the He-Ca separation, which is found when the system evolves from the isosceles A to the quasilinear A configuration. In this sense, the larger contribution from the latter structures to the overall geometry of the ground state of Ca-^{3}He$_2$ than for the ^{4}He case could be compatible with the shift of the maximum to larger distances in the probability density function of the former system (see left bottom panel of Fig. 2). These estimates are nevertheless far from being definitive since the classification

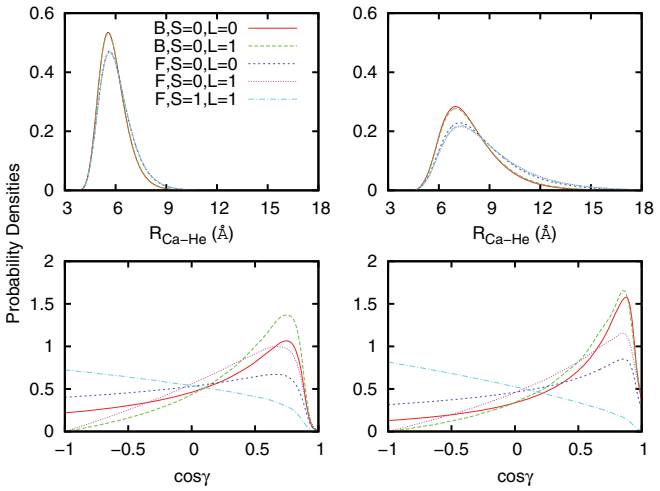

FIG. 6. (Color online) DVR radial Ca-He distributions (upper panels) and angular distributions (lower panels) of the $v = 0$ ground vibrational states for the indicated S, L combinations. B: bosonic system; F: fermionic system. Left panels: Ca-He interaction from Ref. [15]; right panels: that from Ref. [14].

of the basis functions of the DGF calculation into the different geometrical families is subject to some arbitrariness in the comparison of the different sizes of the triangle. In addition, for the description of the overall structure, the quantitative presence of each type of triangle in the basis set depends on a ratio generated by the acceptance procedure to include or not include the corresponding ϕ_j functions.

As already mentioned, besides the scalene type, which turns out to be the most abundant geometry for both isotopic variants, those isosceles triangles with the Ca atom in between the two He atoms play a significant role in the overall structure of the ground bound state. In particular, those isosceles in which the $\cos\gamma$ is negative, meaning that the calcium atom approaches the He-He axis and which eventually may become quasilinear A, imply a contribution of $\sim$12% to the overall geometry in the case of ^{4}He and $\sim$13% for ^{3}He. If we add these values to the contribution shown for the quasilinear A type in Table IV, we can conclude that the transition between these kinds of linear structures and the isosceles A type is playing a more important role for the fermionic case than in the bosonic cluster.

D. $L = 1$, $S = 0, 1$ trimers

We have also investigated rotationally excited $L = 1$ states through DVR calculations. Three bound states were obtained for bosons and triplet fermions, while the singlet fermionic complex only supports two bound levels. The associated energies are listed in Table V, where the corresponding ε, κ symmetry quantum numbers for each system are also included. Note that the $L = 1$ triplet fermionic ground state presents a higher binding energy than the singlet when the Ca-He potential of Ref. [15] is used, while for that of Ref. [14], the situation is the reverse. For $v = 0$ ground vibrational states, and for the combinations $S = 0, 1$ and $L = 0, 1$ of bosonic and fermionic Ca-He$_2$ complexes, we display DVR radial Ca-He distributions in the upper panels of Fig. 6. As can be seen, the distributions for the bosonic system, and those of the fermionic one, are independent of the rotational or of the spin state. Additionally, the associated angular distributions are shown in the lower panels of that figure: it is worth mentioning that for the bosons, as well as for singlet fermions, the distributions are more peaked near small angles for rotationally excited states, $L = 1$, than those corresponding to $L = 0$, i.e., the rotational excitation enhances the tendency of He atoms to pack themselves closer to each other, leaving outside the Ca impurity. The scenario for the $L = 1$ triplet fermionic system is just the reverse: the ^{3}He atoms tend to locate in a collinear He-Ca-He arrangement, which is a signature of the onset of solvation.

In addition, we have also investigated the case of the rotating bosonic system by means of the DGF approach described in Sec. III B. For the Kleinekathöfer Ca-He potential, the values of the rovibrational energies are -7.7320, -6.6077, and -5.1124 cm^{-1}, respectively, and for the PES of Ref. [14], only a bound state of energy -0.9940 cm^{-1} is observed. The states selected from the DGF calculation for such a comparison are those corresponding to $|\Omega| = 1$ with the closest proximity in energy with respect to the DVR results. No further consideration regarding the possible symmetry of those states have been taken into account, given the different description employed in the DVR and the DGF calculations. The agreement between both sets of data is nevertheless quite satisfactory.

Simulated absorption spectrum

A more precise evaluation of the difference between the two Ca-He interactions [14,15] can be achieved through the corresponding absorption spectra. For the bosonic complex, taking into account ground ($L = 0$) and first excited ($L = 1$) rotational states, instead of using Eq. (7) we have resorted to simulating the spectra as the allowed lines of intensity,

$$I(v'L' \leftarrow vL) \propto \left|\left\langle p_{Lv}(\cos\gamma) D^{1/2}_{Lv}(\cos\gamma) | \cos(\gamma/2) | p_{L'v'}(\cos\gamma) D^{1/2}_{L'v'}(\cos\gamma)\right\rangle\right|^2, \tag{24}$$

where D are the corresponding angular distributions and $\cos\gamma$-dependent phases $p = \pm 1$ have been imposed taking advantage of the clear nodal structure exhibited by the $\cos\gamma$ distributions for vibrationally excited states. These distributions, for the main states involved, are shown in the lower panels of Fig. 7, depending on the Ca-He interaction

TABLE VI. Simulated absorption microwave spectrum of the Ca-$^4He_2$ system. Photon energies (cm^{-1}) and intensity of lines (arbitrary units) depending on the Ca-He interaction used: columns 2–3, Ref. [15]; columns 4–5, Ref. [14].

	$\hbar\omega$	I	$\hbar\omega$	I
R_{00}	0.26	0.6035	0.1754	0.688
P_{01}	0.41	8.67(−2)	0.1757	5.01(−2)
R_{11}	0.69	0.2798		
P_{12}	0.75	0.1528		
P_{23}[a]	0.85	0.2578		
R_{22}	1.04	0.2647		
R_{01}	1.36	3.20(−3)		
P_{02}	1.85	3.93(−4)		
R_{12}	2.48	9.90(−4)		
P_{13}[a]	2.64	2.91(−2)		
R_{02}	3.15	5.80(−4)		
P_{03}[a]	3.74	2.65(−2)		

[a]These lines are less reliable.

considered. In the lower right panel of that figure, the modeled dipole moment $\mu = \cos(\gamma/2)$ is also depicted. The upper panels of Fig. 7 display the radial Ca-He distance distributions and support the modeling of the dipole moment considered (see above), leading to transitions between states of the bending mode. The state ($L = 0$, $v = 3$), depicted in Figs. 3 and 4 but not here, constitutes an exception as it clearly shows a mixed stretching-bending excitation. Hence, intensities of lines corresponding to transitions involving this state become less reliable. The results for the main $L' = L \pm 1$ transitions are listed in Table VI and are in part displayed in Fig 8. The notation $R_{vv'}$ corresponds to transitions $(L = 1, v') \leftarrow (L = 0, v)$, while $P_{vv'}$ denotes a transition $(L = 0, v') \leftarrow (L = 1, v)$. As can be seen, the resulting spectra belong to the microwaves region. Owing to the different triatomic states produced by the use of one or the other interaction, it is evident

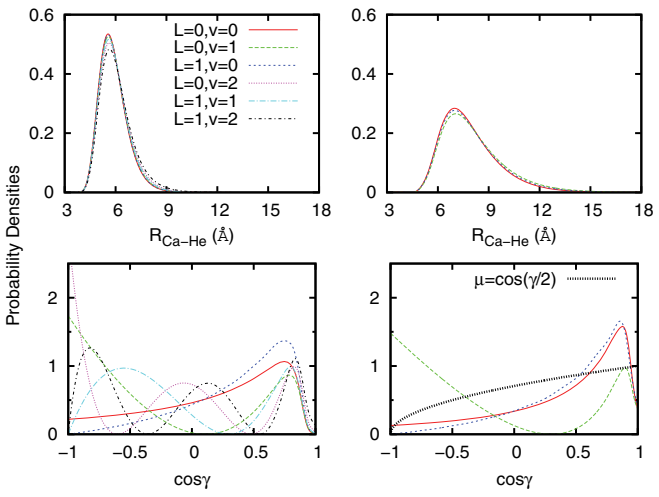

FIG. 7. (Color online) Radial (upper panels) and angular (lower panels) distributions for the main bosonic states involved in dipole transitions. Left panels: Ca-He interaction from Ref. [15]; right panels: that of Ref. [14]. In the right lower panel, the dipole moment has been also included.

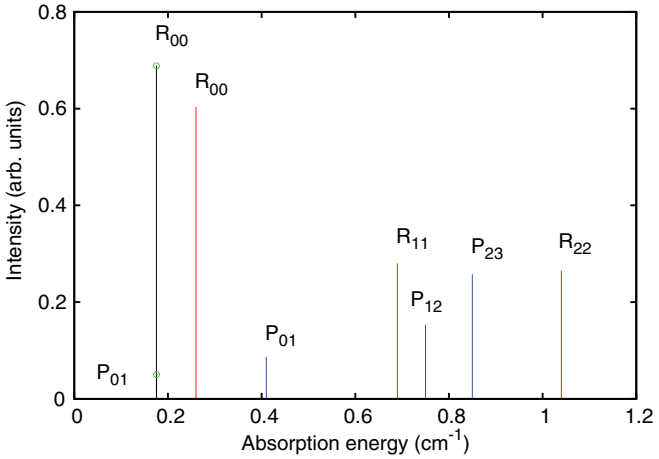

FIG. 8. (Color online) Simulated absorption microwave spectrum of the Ca-$^4He_2$ system. The black lines (green points) on the left correspond to the only two transitions appearing when the Ca-He interaction of Ref. [14] is used. The resting lines correspond to the spectrum produced by using the Ca-He interaction of Ref. [15].

that the Kleinekathöfer potential [15] gives rise to a richer spectrum than that coming from the Lovallo-Klobukowski one [14], with the latter presenting just a couple of lines (R_{00} and P_{01}) almost degenerate in energy. The interaction of Ref. [15], in turn, separates these two lines by a measurable amount of 0.15 cm^{-1}, although the respective intensities are very similar. Also, noticeable additional R and P lines are provided by this potential, extending up to the P_{03} one at 3.74 cm^{-1}.

V. CONCLUDING REMARKS

We have investigated the weakly bound states of bosonic Ca-$^4He_2$ and fermionic Ca-$^3He_2$ triatomic complexes using three different methods (DMC, DGF, and DVR) and the same potential recently employed by Gou and Li [16] consisting of the addition of He-He [19] and Ca-He [15] interactions. Bound energies and corresponding spatial distributions were presented and discussed. In the nonrotating $L = 0$ scenario, the triplet fermionic system does not exist, and only four (three) bosonic (singlet fermionic) vibrational bound states were found. The present results, which are essentially the same independent of the method we applied, substantially differ from those reported in Ref. [16], a difference which we have not been able to explain. We have further considered a different Ca-He [14] interaction, maintaining the pairwise description of the potential with the same He-He interaction [19], and compared the results with those obtained by the use of that of Ref. [15]. For both potentials, in the ground $L = v = 0$ state, bosonic He atoms show a propensity to pack closer to each other, leaving outside the Ca atom, whereas fermionic He atoms explore near collinear He-Ca-He arrangements, a feature which may constitute a signature of a solvation process. This scenario is found to be more pronounced in the case of the potential of Lovallo-Klobukowski [14] than that of Kleinekathöfer [15].

For L=1, the bosonic system, as well as the triplet fermionic one, presents three bound levels, and the singlet fermionic

complex supports two bound states when the Ca-He interaction of Ref. [15] is used, while each of these species presents only one bound level employing the Ca-He potential of Ref. [14]. The corresponding ground vibrational states show that independent of the mass and the interaction used, the packing of He atoms at $S = 0$ is favored by rotational excitation. On the contrary, in the ground vibrational state of the triplet fermionic complex, the He atoms tend to solvate the Ca impurity.

Although both potentials give rise to similar geometrical considerations for ground rovibrational states, simulated absorption spectra in the microwaves region clearly discriminate between them, thereby being helpful to determine their relative feasibility for realistically representing the required interaction forces.

ACKNOWLEDGMENTS

We thank Centro de Cálculo (IFF, CSIC), Centro Técnico de Informática (CTI, CSIC), and Centro de Supercomputación de Galicia (CESGA) for the allocation of computer time. This work has been supported by MICINN, Grants No. FIS2010-18132 and No. FIS2011-29596-C02-01. R.R.-C. and D.L.-D. acknowledge the Spanish programs JAE-PREDOC, Grant No. JAE-Pre-2010-01277, and JAE-DOC, Contract No. E-28-2009-0448699, respectively. F.A.G. thanks the PRIN project 2009 for financial support. The aid of COST Actions CM1002 (CODECS) and MP1002 (Nano-IBCT) are also appreciated.

[1] J. P. Toennies and A. F. Vilesov, Angew. Chem. Int. Ed. **43**, 2622 (2004).

[2] S. Grebenev, J. P. Toennies, and A. F. Vilesov, Science **279**, 2083 (1998).

[3] F. Stienkemeier and A. F. Vilesov, J. Chem. Phys. **113**, 10119 (2001).

[4] M. Y. Choi, G. E. Douberly, T. M. Falconer, W. K. Lewis, C. M. Lindsay, J. M. Merritt, P. L. Stiles, and R. E. Miller, Int. Rev. Phys. Chem. **25**, 15 (2006).

[5] R. N. Barnett and K. B. Whaley, Phys. Rev. A **47**, 4082 (1993).

[6] F. Ancilotto, P. B. Lerner, and M. W. Cole, J. Low Temp. Phys. **101**, 1123 (1995).

[7] F. Ancilotto, E. Cheng, M. W. Cole, and F. Toigo, Z. Phys. B: Condens. Matter **98**, 323 (1995).

[8] J. Reho, U. Merker, M. R. Radcliff, K. K. Lehmann, and G. Scoles, J. Chem. Phys. **112**, 8409 (2000).

[9] F. Stienkemeier, F. Meier, and H. O. Lutz, J. Chem. Phys. **107**, 10816 (1997).

[10] F. Stienkemeier, F. Meier, and H. O. Lutz, Eur. Phys. J. D **9**, 313 (1999).

[11] E. Loginov and M. Drabbels, J. Chem. Phys. **136**, 154302 (2012).

[12] A. Hernando, R. Mayol, M. Pi, M. Barranco, F. Ancilotto, O. Bünermann, and F. Stienkemeier, J. Phys. Chem. A **111**, 7303 (2007).

[13] O. Bünermann, M. Dvorak, F. Stienkemeier, A. Hernando, R. Mayol, M. Pi, M. Barranco, and F. Ancilotto, Phys. Rev. B **79**, 214511 (2009).

[14] C. C. Lovallo and M. Klobukowski, J. Chem. Phys. **120**, 246 (2004).

[15] U. Kleinekathöfer, Chem. Phys. Lett. **324**, 403 (2000).

[16] Q. Gou and Y. Li, Phys. Rev. A **85**, 012510 (2012).

[17] D. David López-Durán, T. González-Lezana, G. Delgado-Barrio, P. Villarreal, and F. A. Gianturco, Phys. Rev. A **86**, 016501 (2012).

[18] D. López-Durán, R. Rodríguez-Cantano, T. González-Lezana, G. Delgado-Barrio, P. Villarreal, and F. A. Gianturco, Eur. Phys. J. D **66**, 198 (2012).

[19] R. A. Aziz and M. J. Slaman, J. Chem. Phys. **94**, 8047 (1991).

[20] I. Baccarelli, G. Delgado-Barrio, F. A. Gianturco, T. González-Lezana, S. Miret-Artés, and P. Villarreal, Phys. Chem. Chem. Phys. **2**, 4067 (2000).

[21] G. A. Natanson, G. S. Ezra, G. Delgado-Barrio, and R. S. Berry, J. Chem. Phys. **81**, 3400 (1984).

[22] J. T. Muckerman, Chem. Phys. Lett. **173**, 200 (1990).

[23] P. Villarreal, O. Roncero, and G. Delgado-Barrio, J. Chem. Phys. **101**, 2217 (1994).

[24] T. González-Lezana, S. Miret-Artés, G. Delgado-Barrio, P. Villarreal, J. Rubayo-Soneira, I. Baccarelli, F. Paesani, and F. Gianturco, Comp. Phys. Comm. **45**, 156 (2002).

[25] I. Baccarelli, F. A. Gianturco, T. González-Lezana, G. Delgado-Barrio, S. Miret-Artés, and P. Villarreal, Phys. Rep. **452**, 1 (2007).

[26] T. González-Lezana, J. Rubayo-Soneira, S. Miret-Artés, F. A. Gianturco, G. Delgado-Barrio, and P. Villarreal, Phys. Rev. Lett. **82**, 1648 (1999).

[27] F. A. Gianturco, F. Paesani, I. Baccarelli, G. Delgado-Barrio, T. González-Lezana, S. Miret-Artés, P. Villarreal, G. B. Bendazzoli, and S. Evangelisti, J. Chem. Phys. **114**, 5520 (2001).

[28] I. Baccarelli, F. A. Gianturco, T. González-Lezana, G. Delgado-Barrio, S. Miret-Artés, and P. Villarreal, J. Phys. Chem. A **110**, 5487 (2006).

[29] I. P. Hamilton and J. C. Light, J. Chem. Phys. **84**, 306 (1986).

[30] M. Márquez-Mijares, T. González-Lezana, O. Roncero, S. Miret-Artés, G. Delgado-Barrio, and P. Villarreal, Chem. Phys. Lett. **460**, 417 (2008).

[31] M. Márquez-Mijares, R. Pérez de Tudela, T. González-Lezana, O. Roncero, S. Miret-Artes, G. Delgado-Barrio, P. Villarreal, I. Baccarelli, F. A. Gianturco, and J. Rubayo-Soneira, J. Chem. Phys. **130**, 154301 (2009).

[32] H. W. Kroto, *Molecular Rotation Spectra* (Dover, New York, 1992).

[33] G. W. King, R. M. Hainer, and P. C. Cross, J. Chem. Phys. **11**, 27 (1942).

[34] H. H. Nielsen, Rev. Mod. Phys. **23**, 90 (1951).

[35] C. Eckart, Phys. Rev. **47**, 552 (1935).

[36] A. Ernesti and J. M. Hutson, Chem. Phys. Lett. **222**, 257 (1994).

[37] E. Coccia, E. Bodo, F. Marinetti, F. A. Gianturco, E. Yildrim, M. Yurtsever, and E. Yurtsever, J. Chem. Phys. **126**, 124319 (2007).
[38] E. Bodo, E. Coccia, D. López-Durán, and F. A. Gianturco, Phys. Scr. **76**, C104 (2007).
[39] F. Marinetti, E. Coccia, E. Bodo, F. A. Gianturco, E. Yurtsever, M. Yurtsever, and E. Yildirim, Theor. Chem. Acc. **118**, 53 (2007).
[40] B. L. Hammond, W. A. Lester Jr., and P. J. Reynolds, *Monte Carlo Methods in Ab-Initio Quantum Chemistry* (World Scientific, Singapore, 1994).
[41] F. Paesani, F. A. Gianturco, M. Lewerenz, and J. P. Toennies, J. Chem. Phys. **111**, 6897 (1999).
[42] S. Bovino, E. Coccia, E. Bodo, D. López-Durán, and F. A. Gianturco, J. Chem. Phys. **130**, 224903 (2009).
[43] R. Prosmiti, G. Delgado-Barrio, P. Villarreal, E. Yurtsever, E. Coccia, and F. A. Gianturco, J. Phys. Chem. A **113**, 14718 (2009).
[44] W. Press, B. Flannery, S. Teukolsky, and W. Vetterling, *Numerical Recipes* (Cambridge University Press, Oxford, U.K., 1986).
[45] D. Bresanini, G. Morosi, and M. Mella, J. Chem. Phys. **116**, 5345 (2002).
[46] D. Blume, M. Lewerenz, F. Huisken, and M. Kaloudis, J. Chem. Phys. **105**, 8666 (1996).
[47] R. Rodríguez-Cantano, D. López-Durán, T. González-Lezana, G. Delgado-Barrio, P. Villarreal, E. Yurtsever, and F. A. Gianturco, J. Phys. Chem. A **116**, 2394 (2012).